Computation of the Permeability Tensor of Non-Periodic Anisotropic Porous Media from 3D Images

H. Scandelli · A. Ahmadi-Senichault · C. Levet · J. Lachaud

Abstract The direct proportionality between the flow rate and the pressure gradient of creeping flows was experimentally discovered by H. Darcy in the 19th century and theoretically justified a couple of decades ago using upscaling methods such as volume averaging or homogenisation. X-ray computed micro-tomography (CMT) and pore-scale numerical simulations are increasingly being used to estimate the permeability of porous media. However, the most general case of non-periodic anisotropic porous media still needs to be completely numerically defined. Pore-scale numerical methods can be split into two families. The first family is based on a direct resolution of the flow solving the Navier-Stokes equations under the assumption of creeping flow. The second one relies on the resolution of an indirect problem - such as the closure problem derived from the volume averaging theory. They are known to provide the same results in the case of periodic isotropic media or when dealing with representative element volumes (REV). To address the most general case of non-periodic anisotropic porous media, we have identified four possible numerical approaches for the first family and two for the second. We have compared and analysed them on three-dimensional generated geometries of increasing complexity, based on sphere and cylinder arrangements. Only one, belonging to the first family, has been proven to remain rigorously correct in the most general case. This has been successfully applied to a high-resolution 3D CMT of Carcarb, a carbon fiber preform used in the thermal protection systems of space vehicles. The study concludes with a detailed analysis of the flow behaviour (streamlines and vorticity). A quantitative technique based on a vorticity criterion to determine the characteristic length of the material is proposed. Once the characterized length is known, the critical Reynolds number can be estimated and the physical limit of the creeping regime identified.

Institute of Mechanical Engineering of Bordeaux (I2M): University of Bordeaux, ENSAM, INRAe, CNRS, Bordeaux INP.

Keywords Porous media · Permeability tensor · Pore-scale numerical simulations · Micro-CT image · Calcarb · Characteristic length scale

Nomenclature

Latin Letters

$\underline{\underline{K}}$	permeability tensor $[m^2]$
$\underline{\underline{d}}$	velocity deviation tensor $[m\ s^{-1}]$
$\underline{\underline{I}}$	identity tensor
e	pressure deviation term $[Pa]$
r	position vector $[m]$
U	Darcy-scale velocity $[m\ s^{-1}]$
u	pore-scale velocity $[m\ s^{-1}]$
w	pore-scale vorticity $[s^{-1}]$
A	interface area $[m^2]$
c	artificial compressibility coefficient $[m^{1/2}s^{-1/2}]$
ℓ	reference length $[m]$
N	total number of values predicted by the strategies
P	Darcy-scale pressure $[Pa]$
p	pore-scale pressure $[Pa]$
V	Volume $[m^3]$

Greek Letters

δ	thickness of the lateral fluid layer used in strategy B and D $[m]$
ϵ	porosity of the medium
θ	rotation angle
μ	dynamic viscosity $[Pa\ s]$
ρ	pore-scale density $[kg\ m^{-3}]$
ν	kinematic viscosity $[m^2 s^{-1}]$

Symbols

$*$	non-dimensional variable
$\sim$	deviation term

Subscripts and Superscripts

art	artificial
avg	average
cl	cluster
dg	diagonal
f	fluid
s	solid

Acronyms

CMT	Computed Micro-Tomography
$PATO$	Porous material Analysis Toolbox based on OpenFoam
REV	Representative Element Volume

Adimensional Groups

Re	Reynolds number

quantity	dimensionless variable
length	$r^* = r/\ell$ and $\nabla^* = \ell\nabla$
velocity	$u^* = u/U$
pressure	$p^* = p\ell/(\mu U)$

Table 1 Non-dimensional variables for making Eq. (1) dimensionless.

1 Introduction

At the pore scale, the flow of a Newtonian and incompressible fluid in a solid porous medium is described by the Navier-Stokes equations. Under the assumption of steady-state flow and negligible volume forces, these equations become

$$\begin{cases} \nabla \cdot \boldsymbol{u} = 0 \\ \nabla \cdot (\rho \, \boldsymbol{u} \otimes \boldsymbol{u}) - \nabla \cdot (\mu \nabla \boldsymbol{u}) = -\nabla p \\ BC: \quad \boldsymbol{u} = \boldsymbol{0} \quad at \ A_{fs} \end{cases} \tag{1}$$

where ρ and μ denote the density and the dynamic viscosity of the fluid, $\boldsymbol{u}$ and p the pore-scale velocity and pressure, and A_{fs} the fluid-solid area interface. The above system of equations may be written in a non-dimensional form by introducing the dimensionless variables reported in Table 1. In order to completely define them, three reference values need to be chosen. In porous media, the reference velocity, U, is taken as the magnitude of the average velocity in the domain [1]. For the reference length, ℓ, the choice is not trivial as porous micro-structures are very diverse and better characterised by different lengths. The most widely adopted in the modern literature is the porous medium grain diameter [69]. Once the dimensionless variables have been introduced, Eq. (1) can be written as

$$\begin{cases} \nabla^* \cdot \boldsymbol{u}^* = 0 \\ Re \, \nabla^* \cdot (\boldsymbol{u}^* \otimes \boldsymbol{u}^*) - \nabla^{*2}\boldsymbol{u}^* = -\nabla^* p^* \\ BC: \quad \boldsymbol{u}^* = \boldsymbol{0} \quad at \ A_{fs} \end{cases} \tag{2}$$

where Re is the Reynolds number defined as

$$Re = \frac{\rho \, U \, \ell}{\mu} \tag{3}$$

The Reynolds number characterizes the relative importance of inertial and viscous forces within a fluid. For $Re \ll 1$, viscous forces dominate and the flow is said to be in the creeping regime, also known as the Darcy regime. In this regime, a generalized form of Darcy's law finds its validity at the macroscopic scale and the system of Eq. (2) becomes [65]

$$\begin{cases} \nabla \cdot \boldsymbol{U} = 0 \\ \boldsymbol{U} = -\dfrac{1}{\mu} \underline{\underline{\boldsymbol{K}}} \cdot \nabla P \end{cases} \tag{4}$$

Pore-Scale
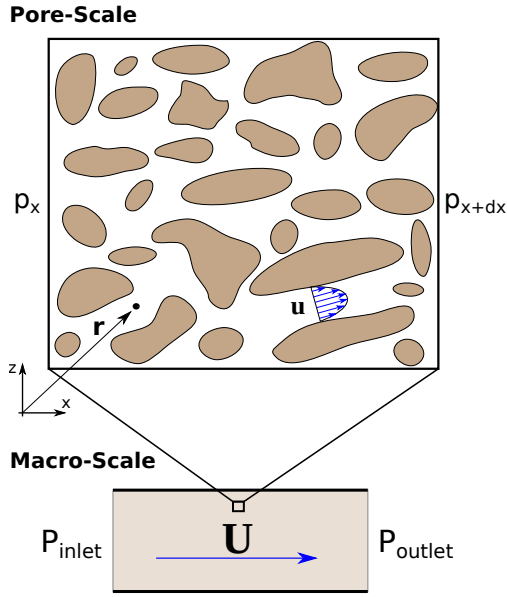
Macro-Scale

Fig. 1 Pore-scale and macro-scale descriptions of the transport problem in porous media.

where P and $\boldsymbol{U}$ are the macroscopic pressure and velocity (see Appendix A) and $\underline{\underline{\boldsymbol{K}}}$ is the permeability tensor. However, when increasing the Reynolds number inertial forces are no longer negligible and Darcy's law loses its validity. Extensions to Darcy's law have been proposed to capture the physics of inertial [21,35,66], transition (unsteady laminar) [1], and turbulence regimes [69].

For most engineering applications related to transport processes in porous media, macroscopic models are used to evaluate the macroscopic pressure and velocity fields [8,18,22,38,56,61,71]. In this way the physics of the problem are greatly simplified as shown in Fig. 1. Simplifications come from the introduction of macroscopic properties, such as the permeability tensor, that enclose information about the microscopic interactions between the flow and the material. The counterpart is a loss of information: the pore-scale approach provides the detailed velocity and pressure fields from the direct resolution of Eq. (1) whereas the macro-scale one only provides averaged (macroscopic) values of these two fields from the resolution of macroscopic models, such as the Darcy model presented in Eq. (4). One important advantage that emerges from the micro-scale studies is the possibility of visualizing the flow behaviour in digital images. The study of streamlines and pressure gradients throughout the domain brings very rich insight. This quantitative microscopic information can be used to better define the characteristic length ℓ as well as to introduce physical parameters as transition criterion, such as the maximum local vorticity. This quantity will be used in this article to derive a new criterion for the validity of Darcy's law.

The objective of this work is to establish and validate a numerical strategy to estimate the anisotropic permeability tensor. This tensor is an essential input to the macroscopic models. It can be determined in several ways. Obviously, experiments can be performed to infer the effective properties. To-date, this remains the most reliable and preferred way [7,44,47,54,60]. With the generalization of super-computers during the last two decades, on the one hand the developing of pore-network models and the possibility to perform lightweight simulations on common laptop, on the other hand numerical simulations have progressively gained popularity for the computation of effective properties [26, 27,34,62]. They are particularly useful to study conditions not accessible in the laboratory [13]. Digitalized geometries of porous media can be obtained either by an idealized mathematical representation or by a reconstructed digital image. In the first case the pore structure is described from a statistical point of view [24] and then reconstructed by means of small primitive objects within a finite domain [64]. Finally, numerical simulations can be performed in order to obtain approximation of the effective properties [17,20,33,63,64]. In the second case actual digital images are obtained, typically by X-ray CMT [3,39], and simulations can be performed on the precise geometries. Porous ceramic [25,30,49], metal foams [12,53], fibrous materials [13,46], and rock samples [51,58], are just some examples of the materials that have already been analyzed using this approach.

Regardless of the method used to produce the digital image, pore-scale numerical simulations need to be defined in terms of computational domains and boundary conditions. In this article, we denote as *strategy* a generic numerical setting in terms of the considered domain (sample) and the boundary conditions of a pore-scale simulation. It is a well-known fact [23,29,50] that the latter need to be chosen carefully as they strongly impact the results if the sample scale is not a representative element volume (REV). The strategies proposed in the literature are presented in Fig. 2 where computational domains are represented in two dimensions for an easier comprehension. Different comments on the strategies may be made:

– The strategies can be split into two families: strategies A [32,42,49,68], B [29], C, and D1 [5,11,24,29], which aim to determine the permeability tensor from Darcy's law where pressure and velocity terms are obtained by solving the Navier-Stokes equations with $Re \ll 1$ and then properly averaged; strategies D2 [29] and E [11,24,29] which aim to determine the tensor by solving the closure problem derived from upscaling techniques [10,65];
– In strategies B, C, D1/2, and E, periodic boundary conditions are imposed on the pressure deviation (see appendix A) and on the velocity field [29];
– In strategies A, B, and C, the effective domain is enclosed between two buffer domains in order to avoid inlet/outlet boundary effects. The averaging of the flow properties is performed only inside the effective domain;
– In strategies B, D1, and D2, a layer of pure fluid of a thickness δ is added between the effective domain and the boundaries in order to enforce pe-
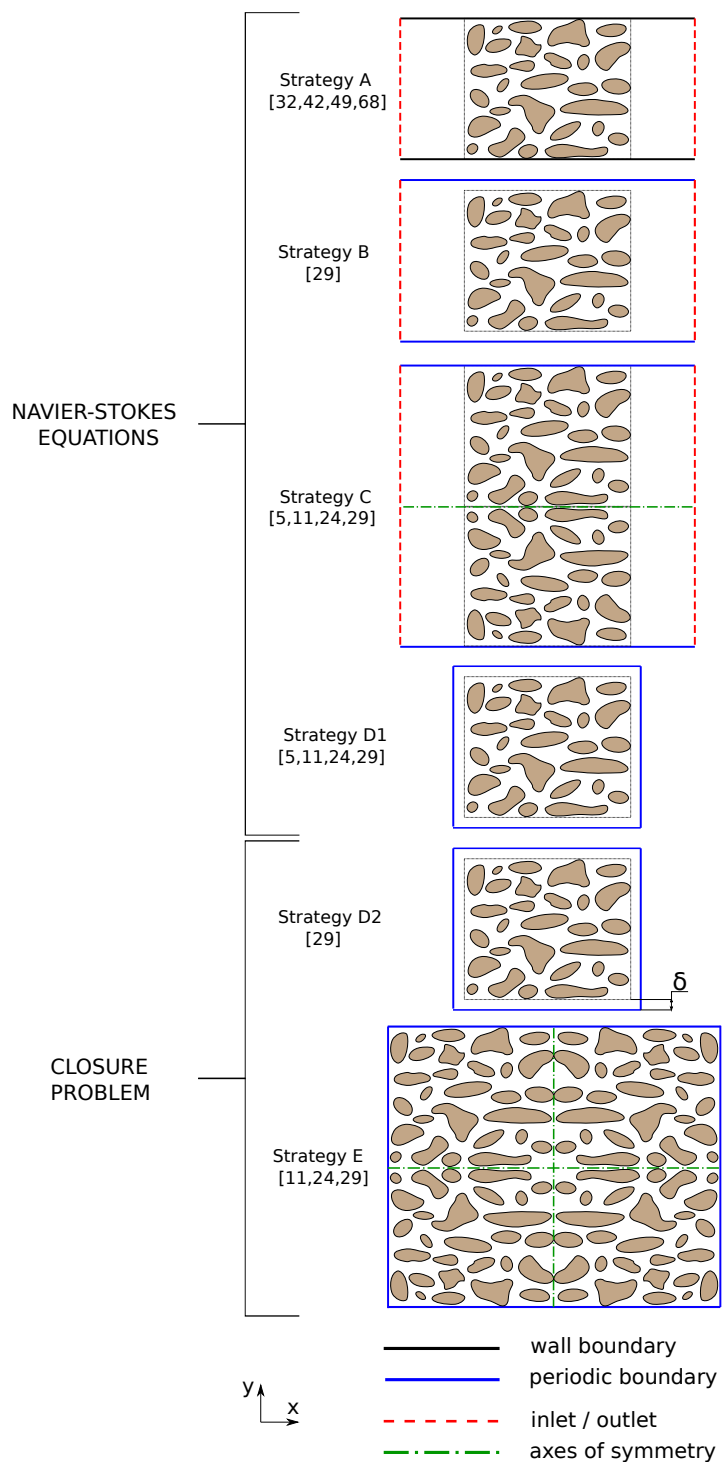
Fig. 2 2D sketches of the computational domains of the six selected strategies between the most used in the literature.

riodic boundary conditions. The thickness, δ, should be large enough to make the domain periodic, but small enough to avoid any possible influence on the problem. To be noticed that for periodic domains δ could also be set equal to zero.

- In strategy E, the domain is made periodic by means of three symmetry operations (one for each axis); in strategy C, the domain is made symmetric on the direction orthogonal to the flow (in the figure, planes with normal vectors in the y and z directions).

The choice of the strategy to adopt depends on the studied porous medium. This aspect has been highlighted numerous times in the literature. Pickup et al, 1994 [50], investigated the impact of several flow models on the calculation of the permeability tensors for sedimentary structures. They demonstrated that periodic boundary conditions are reliable in the example problems considered and that in many cases the differences between the various methods were slight. However, periodic boundary conditions can be considered only for periodic media or when dealing with volumes large enough to be considered as REV. For the other cases, a non-periodic strategy needs to be defined. Manwart et al, 2002 [41], analyzed and compared the accuracy of two different numerical algorithms (one based on the lattice-Boltzmann method and the other on finite-difference techniques) for computing the permeability of three-dimensional porous media. They argued in favour of the finite difference code for different reasons. A relevant study on the estimation of the effects of the boundary conditions on the numerical simulations has been proposed by Guibert et al, 2016 [29]. They selected strategy A with fixed pressure boundary conditions as the most suitable one in the case of 2D periodic synthetic porous media. A further step in this analysis has been proposed by Gerke et al, 2019 [23], where they investigated possible strategies to capture the tensorial nature of the permeability tensor when dealing with periodic stochastic reconstructions of porous media. They came to the conclusion that strategy D was the only way to obtain symmetric permeability tensor that preserved traversal fluxes.

The main objective of this work is to define for the first time a complete numerical procedure to estimate the permeability tensor of non-periodic anisotropic porous media when dealing with volumes not large enough to be considered as REV. A mathematical description of the two families of approaches presented in the introduction is given in Section 2. In Section 3, the six possible strategies are fully described and down-selected thanks to comparisons against well-known elementary test cases, such as beds of spheres and cylinders. Actually, only strategy A was found to provide correct predictions in the most general case of anisotropic non-periodic porous media. In Section 4, this strategy is applied to estimate the permeability tensor of a carbon fiber preform, called Calcarb, and compared with data from the literature. This section also introduces, verifies, and applies a microscopic criterion based on the vorticity to estimate the limit of validity of the creeping regime. We show that the study of the vorticity at the pore scale also helps to identify the proper characteristic

length of the domain. Conclusions of the work are finally presented in Section 5.

2 Mathematical Description of the Two Families of Approaches

As introduced before, there are two families of approaches that can be used to estimate the permeability tensor.
The first family relies on direct simulations at the pore-scale using Eq. (1). Pressure gradients and velocity components are then averaged at the macroscopic scale and substituted into Darcy's law. The latter is conveniently decomposed into the following system

$$
\begin{cases}
U_x = -\dfrac{1}{\mu}\big(K_{xx}\nabla P_x + K_{xy}\nabla P_y + K_{xz}\nabla P_z\big) \\[2mm]
U_y = -\dfrac{1}{\mu}\big(K_{yx}\nabla P_x + K_{yy}\nabla P_y + K_{yz}\nabla P_z\big) \\[2mm]
U_z = -\dfrac{1}{\mu}\big(K_{zx}\nabla P_x + K_{zy}\nabla P_y + K_{zz}\nabla P_z\big)
\end{cases}
\tag{5}
$$

Following the pore-scale simulations, the components of the macroscopic velocity, U_x, U_y, U_z are obtained as averaged values over the domain and the components of the pressure gradients across the material, $\nabla P_x, \nabla P_y, \nabla P_z$, are obtained from the averaged pressure values over the boundaries and the domain sizes in the x, y, z directions. The remaining unknowns of the system are the nine permeability components, namely $K_{xx}, K_{xy}, ..., K_{zz}$. Therefore, in order to have a closed system, it is necessary to perform a total of three simulations by considering three different flow directions. In this way a global system of nine equations can be defined such as shown in Eq. (6), where the

$$
\begin{bmatrix}
U_{D_x}^1 \\
U_{D_y}^1 \\
U_{D_z}^1 \\
U_{D_x}^2 \\
U_{D_y}^2 \\
U_{D_z}^2 \\
U_{D_x}^3 \\
U_{D_y}^3 \\
U_{D_z}^3
\end{bmatrix}
= -\frac{1}{\mu}
\begin{bmatrix}
\nabla P_x^1 & \nabla P_y^1 & \nabla P_z^1 & 0 & 0 & 0 & 0 & 0 & 0 \\
0 & 0 & 0 & \nabla P_x^1 & \nabla P_y^1 & \nabla P_z^1 & 0 & 0 & 0 \\
0 & 0 & 0 & 0 & 0 & 0 & \nabla P_x^1 & \nabla P_y^1 & \nabla P_z^1 \\
\nabla P_x^2 & \nabla P_y^2 & \nabla P_z^2 & 0 & 0 & 0 & 0 & 0 & 0 \\
0 & 0 & 0 & \nabla P_x^2 & \nabla P_y^2 & \nabla P_z^2 & 0 & 0 & 0 \\
0 & 0 & 0 & 0 & 0 & 0 & \nabla P_x^2 & \nabla P_y^2 & \nabla P_z^2 \\
\nabla P_x^3 & \nabla P_y^3 & \nabla P_z^3 & 0 & 0 & 0 & 0 & 0 & 0 \\
0 & 0 & 0 & \nabla P_x^3 & \nabla P_y^3 & \nabla P_z^3 & 0 & 0 & 0 \\
0 & 0 & 0 & 0 & 0 & 0 & \nabla P_x^3 & \nabla P_y^3 & \nabla P_z^3
\end{bmatrix}
\begin{bmatrix}
K_{xx} \\
K_{xy} \\
K_{xz} \\
K_{yx} \\
K_{yy} \\
K_{yz} \\
K_{zx} \\
K_{zy} \\
K_{zz}
\end{bmatrix}
\tag{6}
$$

exponents $1, 2, 3$ refer to the first, second, and third numerical simulations. For simplicity those simulations can be done such that the inlet flow is aligned with the x, y and finally z directions. Once $\underline{\underline{K}}$ is determined from this system, the symmetry conditions [40] on the extra-diagonal components need to be applied in order to enforce the equality of two components which may differ

slightly from each other. To be noted that even if the real unknowns of the tensor are six, three simulations are required to fully compute them. In order to solve Eq. (6), the matrix of the pressure gradients should be invertible, that is, its determinant should be different from zero. In the creeping regime, an equivalent condition for that is

$$\left(\boldsymbol{U}^1 \times \boldsymbol{U}^2\right) \cdot \boldsymbol{U}^3 \neq 0 \tag{7}$$

The second family of strategies is based on upscaling theories to evaluate the permeability. As long as the same physical hypotheses are used, results coming from the different techniques are the same [16,52]. In this work we have chosen to adopt the volume averaging theory. The method leads to the definition of the following closure problem [10,65]

$$\begin{cases} \nabla e - \nabla^2 \underline{\underline{d}} = \underline{\underline{I}} & in \ V \\ \nabla \cdot \underline{\underline{d}} = 0 & in \ V \\ BC1 : \underline{\underline{d}} = 0 & at \ A_{fs} \\ BC2 : \underline{\underline{d}}(\boldsymbol{r} + \boldsymbol{l_i}) = \underline{\underline{d}}(\boldsymbol{r}), \ \ e(\boldsymbol{r} + \boldsymbol{l_i}) = e(\boldsymbol{r}) & i = 1,2,3 \end{cases} \tag{8}$$

where $\boldsymbol{e}$ is the pressure deviation term (see Appendix A) and $\underline{\underline{d}}$ the velocity deviation tensor. $BC2$ enforces periodic boundary conditions for the two deviation components and the permeability tensor is a function of the velocity deviation tensor as follows
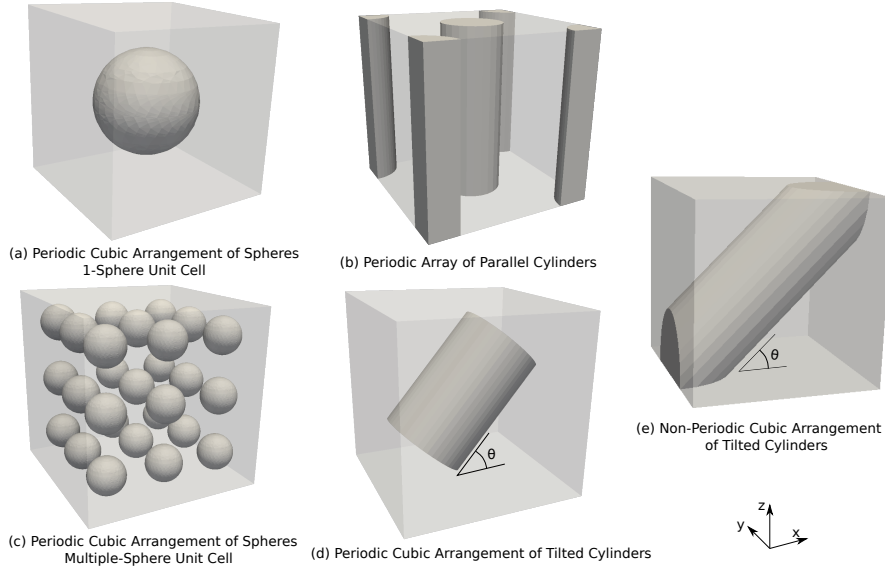
$$\underline{\underline{K}} = -\ \epsilon\ \frac{1}{V} \int_V \underline{\underline{d}}\ dV \tag{9}$$

where ϵ is the porosity of the medium and V the volume of the flow.

In this work, both volume averaging upscaling and direct simulations at the pore-scale are addressed using OpenFoam [57] for the simulations and Paraview [2] for the post-processing. Navier-Stokes equations are solved with SIMPLE [31,48], a steady-state solver for incompressible flow. The closure problem (Eq. (20)) is solved with KclosureSolver (more information in Appendix B), a solver that we have implemented and that is released in the Open Source in the Porous material Analysis Toolbox based on OpenFOAM (PATO) [36,37].

3 Down-Selection of the numerical strategy

We have implemented the six different strategies showed in Fig. 2 with the objective of verifying their validity on simple test cases to select the most suitable one. The simple test cases considered are shown in Fig. 3 and presented in the following sections. Reference values are available in the literature for configurations (a), (b) and (c) [15,55]. We have chosen simple domains with increasing complexity thus allowing us to progressively discard inaccurate strategies. Strategies needed to be defined in terms of boundary conditions for pressure and velocity. Different combinations may be considered. Therefore, to be as

(a) Periodic Cubic Arrangement of Spheres
1-Sphere Unit Cell

(b) Periodic Array of Parallel Cylinders

(c) Periodic Cubic Arrangement of Spheres
Multiple-Sphere Unit Cell

(d) Periodic Cubic Arrangement of Tilted Cylinders

(e) Non-Periodic Cubic Arrangement
of Tilted Cylinders

Fig. 3 Six basic test cases with increasing complexity used to apply, compare, and select the most suitable strategy.

thorough as possible seven sub-strategies have been defined in order to take all combinations into account. They are summarized in Table 2.

In the following sections, strategies are compared between each other and to reference solutions. For such purpose, the following relative error is defined

$$relative\ error = \frac{1}{N} \sum_n^N \frac{K_{ref,n} - K_n}{K_{ref,n}} \, 100 \qquad (10)$$

where K_n is a generic permeability value resulted from the simulation and N is the total number of values predicted by the strategies. As generic indication, strategies will be discarded when their relative error is higher than 25%.

3.1 Periodic Cubic Arrangement of Spheres: 1-Sphere Unit Cell

The unit cell of this domain consists of a solid sphere and a cubic fluid zone (Fig. 3a) thus leading to an isotropic porous medium for which the permeability tensor reduces to a diagonal tensor with equal components ($K = K_{xx} = K_{yy} = K_{zz}$). Four cases are considered, each one characterized by a different sphere radius, hence a different porosity.
The permeabilities computed with strategies A (including the 7 sub-strategies), B, D1, and D2 are plotted in Fig. 4. Strategies C and E are not necessary here as the domain is already symmetric. Permeability values are conveniently

		fixedValue		periodic		slip		no-slip		zero gradient		linear gradient	
	/	u	p	u or $\underline{d}$	p or e	u	p	u	p	u	p	u	p
S A1	inlet	blue											
	outlet		red										
	buffer wall					blue							
	effective wall										red		
S A2	inlet		red										
	outlet												
	buffer wall					blue							
	effective wall										red		
S A3	inlet	blue											
	outlet		red										
	buffer wall							blue					
	effective wall										red		
S A4	inlet	blue											
	outlet		red										
	buffer wall									blue			
	effective wall												red
S A5	inlet	blue											
	outlet		red										
	buffer wall									blue	red		
	effective wall												
S A6	inlet	blue											
	outlet		red										
	buffer wall					blue							
	effective wall									blue	red		
S A7	inlet	blue											
	outlet	red											
	buffer wall							blue					
	effective wall									blue	red		
S B	inlet	blue											
	outlet		red										
	buffer wall			blue	red								
	effective wall			blue	red								
S C	inlet	blue											
	outlet		red										
	effective wall			blue	red								
S D1	inlet			blue	red								
	outlet			blue	red								
	effective wall			blue	red								
S D2	inlet			blue	red								
	outlet			blue	red								
	effective wall			blue	red								
S E	inlet			blue	red								
	outlet			blue	red								
	effective wall			blue	red								

Table 2 List of all the strategies considered determining the permeability. Velocity and pressure settings are indicated respectively in blue and red. For the pressure, *zero gradient* means that the pressure gradient normal to the wall is set to zero. For the velocity, the *slip condition* preserves the velocity tangential to the wall and sets to zero the normal component.

made dimensionless with the square of the unit cube dimension. Mesh refinement has been selected after a convergence analysis (see Appendix C). Several observations can be made:

- Since the domain is symmetric, strategies B, D1, and D2 have been set with $\delta = 0$. Moreover, always because of the symmetry of the domain, strategies C and E are identical to B and D2 respectively;
- The relative error between the reference and strategy D1 and D2 is less than 1%;
- Results from strategies A1 and A2 differ by less than 0.01%. The only difference between them is that strategy A2 displays a longer convergence time (doubled). For this reason strategy A2 is discarded in what follows;
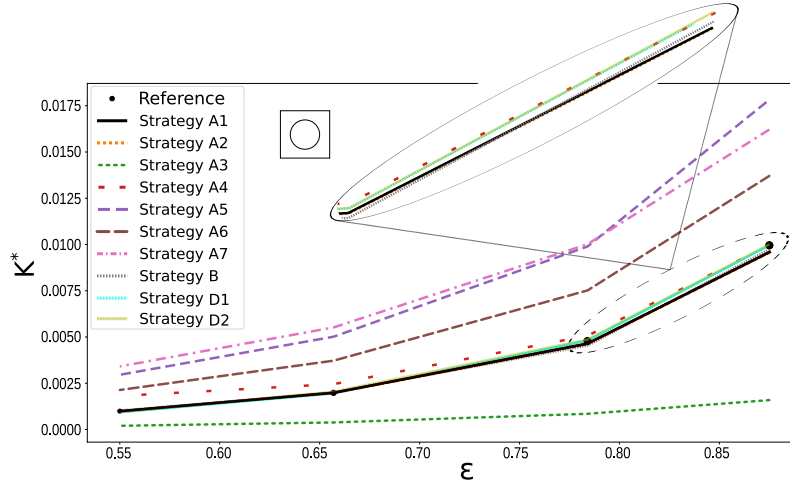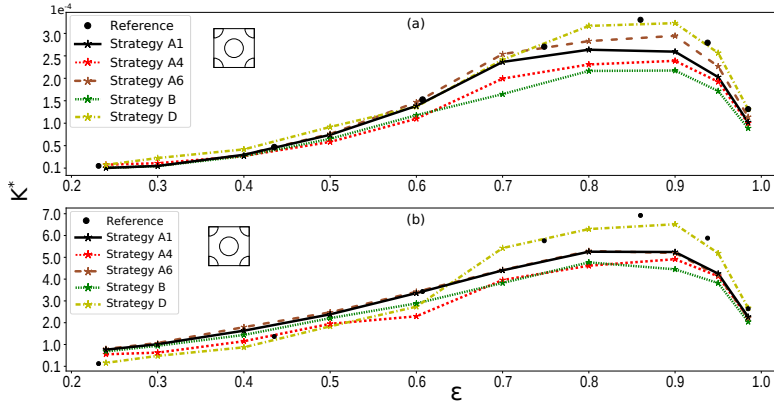
Fig. 4 Dimensionless permeability estimations for the periodic cubic arrangement of spheres obtained by applying the different strategies defined in Table 1, compared to the reference values [15, 55]. One-sphere unit cell has been considered with increasing radius, thus with different porosity values. Permeability values have been made non-dimensional by the square of the unit cube dimension.

• Boundary conditions defined for strategies A3, A5, and A7 are not able to provide accurate predictions in terms of permeability (relative error higher than 25%). They are then discarded;

3.2 Periodic Array of Parallel Cylinders With a Face-Centered Square Arrangement

The unit cell of this periodic orthotropic structure is presented in Fig. 3b. In this case the permeability tensor is characterized by two different values, $K_{xx} = K_{yy}$ and K_{zz}, whereas all the extra-diagonal components are equal to zero. Ten different cases are defined, each characterized by a different value of porosity. The permeability components are estimated using strategies A1, A4, A6, B, D1, and D2. After being made dimensionless by the square of unit cube dimension, they are compared with the reference values in Fig. 5. The domain is symmetric, so strategies C and E are not considered and $\delta = 0$ for strategies B, D1 and D2. Strategies D1 and D2 lead again to a similar description of the problem. Their results differ by 0.1% and that is why we decided to group them under the generic name of Strategy D. Results from strategy D are very accurate, the relative error with the reference is always lower than 5%. Due to its boundary conditions and in particular to the forcing of the periodicity in one direction only, strategy B is not able to accurately capture the orthotropic tensor (relative error around 30%). For this reason it has been discarded.
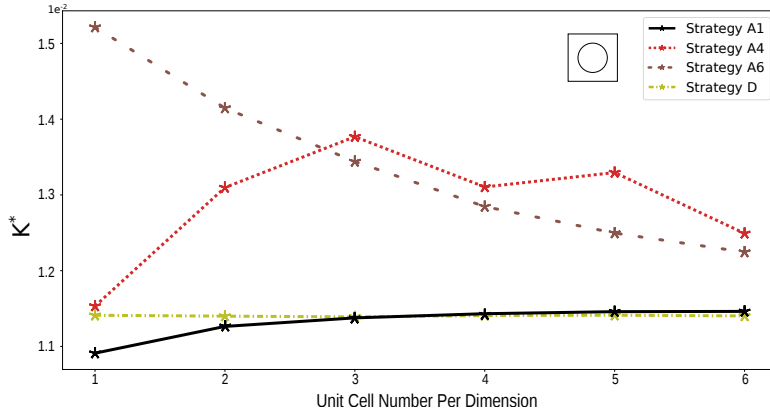
Fig. 5 Dimensionless permeability estimation for the array of parallel cylinders with face-centered square arrangement as a function of the domain porosity: a) Kxx=Kyy, b) Kzz.

3.3 Periodic Cubic Arrangement of Spheres: Multiple-Sphere Unit Cell

This arrangement of spheres is produced by cloning several times the single-sphere unit cell along each direction. Theoretically, the permeability of the domain is the same regardless of the number of single-spheres considered. However, due to the effects of the boundary conditions the estimated permeability values differ as it has been observed above. Indeed, by increasing the domain size, hence the number of spheres, the effect of the boundaries should reduce and the difference between the true and the estimated permeability should tend to zero.

The porosity of each unit is constant and equal to $\epsilon = 0.875$, closer to the porosities expected for the applications we are targeting. Different cases are analyzed, each defined by a different number of unit cells along each direction. In order to make a reasonable comparison, the mesh discretization of a single cell is kept the same regardless of the total number of cells. This makes the size of the mesh to exponentially increase every time a unit cell added and we have stopped after 6 unit cells per direction because of the computational cost. Strategies A1, A4, A6, and D (with $\delta = 0$) are used to estimate the permeability. Once made dimensionless with the square of the unit cube dimension, the results are plotted in Fig. 6. Strategies C and E are not considered since the domain is symmetric. Different observations on the results can be made:

- Strategy D provides constant results with increasing unit-cell numbers, as expected;
- As expected, strategies A1, A4, and A6 have the tendency to converge to the results of strategy D, with relative errors given in Table 3;
- Strategy A4 has a non-monotonous converging rate. A possible explanation is that this boundary condition forces the flow to be aligned to the inlet-outlet axis leading to a wrong velocity field, thus wrong results [24]. By increasing the unit cells in the domain the effects of the boundaries

Fig. 6 Dimensionless permeability estimations for the periodic cubic arrangement of spheres as a function of the number of spheres inside one unit cell.

	1-Cell	2-Cells	3-Cells	4-Cells	5-Cells	6-Cells
STRATEGY A1	4.8 %	1.3 %	0.22 %	0.31 %	0.45 %	0.48 %
STRATEGY A4	1.17 %	16.3 %	22.8 %	16.4 %	18.0 %	10.4 %
STRATEGY A6	36.5 %	26.5 %	19.6 %	13.9 %	10.4 %	8.1 %

Table 3 Relative errors between strategies A with respect to strategy D for the periodic cubic arrangement of spheres by increasing the number of unit cells. By increasing the number of unit cells the relative errors for the different strategies decrease.

start to affect less the field and the estimated permeability converges to the correct value. This strategy has been discarded.

• Strategy A1 has the fastest convergence. This strategy is the one that less affects the simulations and hence the results.

3.4 Periodic Cubic Arrangement of Tilted Cylinders

The unit cell of the periodic porous medium, Fig. 3d, consists of a solid cylinder placed in the middle of the unit cube. It is progressively tilted along the y axes until a full rotation of 90 degrees. It is the simplest periodic test case capable of providing extra-diagonal terms in the permeability tensor. Indeed, the latter is characterized by the three diagonal terms plus the extra-diagonal $K_{xz} = K_{zx}$ components.
Ten different cases are defined, each characterized by a different rotation angle θ. The dimensionless tensors inferred from strategies A1 and A6 have been plotted and compared in Fig. 7. Results from the closure problem (strategy D with $\delta = 0$) are considered here as reference results. Different observations can be made:

• All the strategies correctly predict (error below 10%) the constant values of the K_{yy} component during the rotations;
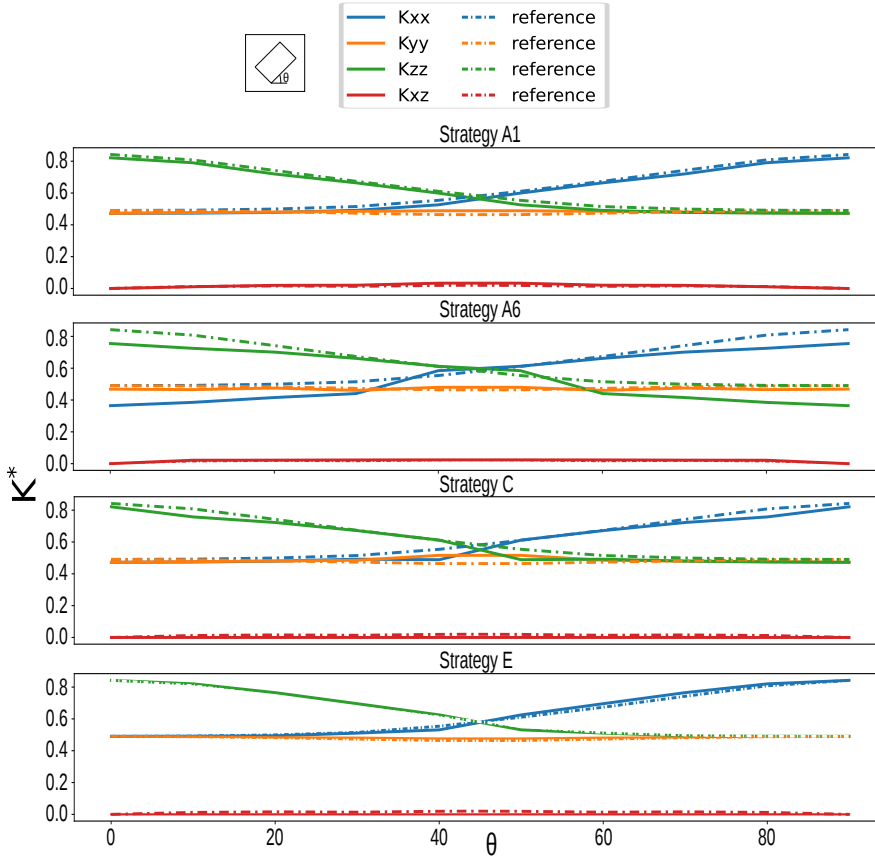
Fig. 7 Dimensionless permeability estimation of the periodic cubic arrangement of tilted cylinders as a function of the orientation angle (θ) for the unit cell of Fig. 3d estimated by different strategies and compared with results of strategy D.

• Strategy A1 predicts diagonal components with a maximum error of 5% and extra-diagonal terms within 10% of error. The error has been observed to remain almost constant for all the rotation angles.

• Strategy A6 correctly predicts the extra-diagonal term (error less than 1%) but not the diagonal ones (higher relative errors with respect of A1). The symmetric condition for the velocity field on the lateral boundaries strongly reduces the anisotropy features inside the domain;

• Strategies C and E lead to a good prediction of the three diagonal components (especially strategy E), but they completely cancel the non-diagonal term: by construction both of them annihilate the transverse flow and kill any anisotropy features inside the domain. So, the use of symmetry operations allow us to use the periodic boundary conditions but at the price of losing the ability to predict extra-diagonal components. For this reason these two strategies have been discarded.
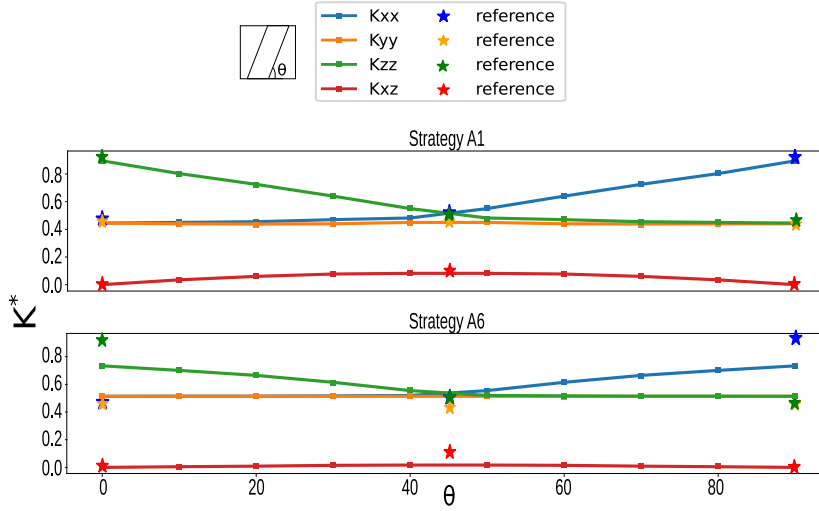
Fig. 8 Dimensionless permeability estimation of the non-periodic cubic arrangement of tilted cylinders as a function of the orientation angle (θ) for the unit cell of Fig. 3e estimated by strategies A1 and A6, while strategy D is used as reference only for the three periodic cases $\theta = 0°, 45°$, and $90°$.

3.5 Non-Periodic Cubic Arrangement of Tilted Cylinders

The last basic test case consists of a non-periodic cubic arrangement of tilted solid cylinders, Fig. 3e. The case is similar to the previous one, with the only difference that now the domain is non-periodic for most of the values of θ, thus, it has been possible to check the strategies on a non-periodic domain in order to be relevant for fibrous media.

As in the previous case, ten different values of the rotation angle are considered and dimensionless permeability results are plotted and compared in Fig. 8. Strategies A1 and A6 are considered and results are verified by means of strategy D with $\delta = 0$ only for those angles that make the domain periodic: $\theta = 0°, 45°$, and $90°$. The generic strategy D with $\delta \neq 0$ is found to be unsuitable in this study. When having small domains (as in this article) the value of δ to make it periodic becomes too big with respect to the domain size to avoid any influence on the results. This strategy has to be discarded for non-periodic media. Again, strategy A1 leads to a prediction with less than 5% of error in the three periodic cases, while the other two lead to errors above 40%.

Thanks to these six cases it has been possible to compare the different strategies. Strategy A1 has been proven to be the only suitable one for generic non-periodic porous materials. It is the only one to predict with a good accuracy both diagonal and extra-diagonal terms of the permeability tensor. The boundary conditions used in this strategy are the ones that less affect the numerical simulations.
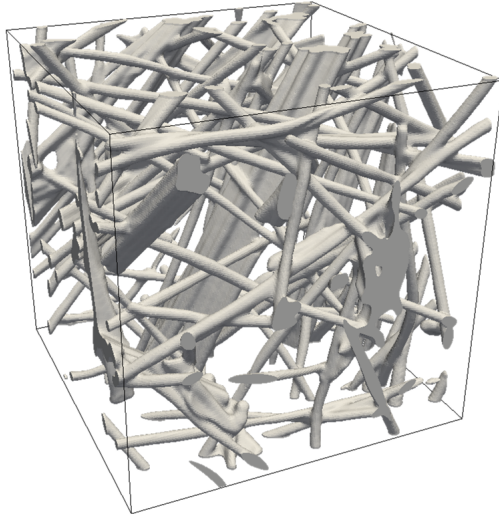
Fig. 9 Volume rendering of the CMT of Calcarb.

## 4 Selected Strategy Applied to an Anistropic Non-Periodic Medium

Now that strategy A1 has been selected to estimate the permeability tensor, let's apply it to a real case. The geometry considered is a sample of virgin Calcarb, illustrated in Fig. 9. Carbon fiber preforms, such as Calcarb [14], are used as skeleton in heat-shield materials [45,59,70] with average porosities higher than 85 %. Its micro-structure is generally characterized by fibers preferentially aligned at about ± 15 degrees with one of the planes and this gives transverse isotropic properties to the material. The digital representation of its micro-structure has been acquired at the Advanced Light Source at Lawrence Berkeley National Laboratory and more details can be found in Borner et al, 2017 [13]. The resulting dataset (Fig. 9) has a resolution of 200 X 200 X 200 voxels, with a voxel size of 2.6 μm. Moreover, the dataset has been characterized in terms of volume fraction as a function of the pore-size in the through-thickness direction, computed using a granulometry method in Geodict. Fig. 10 shows the results of this analysis and in particular the average pore-size in the through-thickness direction for the domain can be estimated to be equal to $\ell_{avg} = 135$ μm. We can conclude that the Calcarb dataset analyzed in this paper (Fig. 9) is too small to be a REV of the material: the size of 520 μm leads to an average of 4 pores for each direction, not enough to guarantee the domain to be representative.
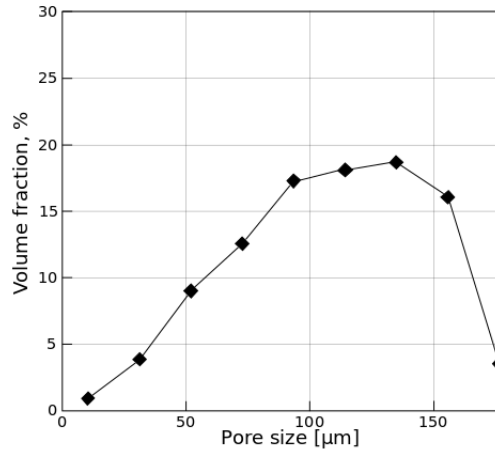
Fig. 10 Granulometry analysis done in Geodict [13]. The average pore-size in the through-thickness direction for the domain can be estimated to be equal to $\ell_{avg} = 135\ \mu m$.

4.1 Mesh Convergence Analysis

The mesh has been created by means of the OpenFoam utility *snappyHexMesh*. This tool can be considered as a mesh sculptor since it requires an already existing base mesh (usually created with the *blockMesh* utility) to chisel it into the desired mesh. The quality of the resultant mesh strongly depends on the tuning of different parameters. For the purpose of this simulation, the parameters are tuned in order to produce a good quality mesh (small values of skewness and non-orthogonality, and aspect ratio close to one) and to define a mesh as homogeneous as possible. Once the parameter configuration process is over, a convergence analysis is required in order to check that the defined mesh does not influence the results. In order to do that, the behaviour of a physical quantity should be monitored by repeating pore-scale numerical simulations with increasingly fine meshes. The pressure difference between the inlet and the outlet is considered as an appropriate criterion to study the convergence, since this quantity is strictly related to the permeability estimation. At this stage these cases will be distinguished by the value of the input velocity and Re values will not be given. A further analysis will allow the proper choice of the characteristic length for the definition of the Reynolds number. Three different inlet velocity values (corresponding to three different Reynolds numbers) are considered in order to include in the mesh analysis both the creeping and the inertial regimes. Indeed, to detect the limit of validity of Darcy's law we need a good mesh in both regimes. The mesh convergence study has been made with pressure residuals lower than 10^{-6} and velocity residuals lower than 10^{-8}. The results of this study are shown in Figs. 11 and 12. In figure 11 it is possible to observe how the monitored quantity converges by refining the mesh. Moreover, for small velocities, cases a) and b), a creeping flow regime is expected thus,
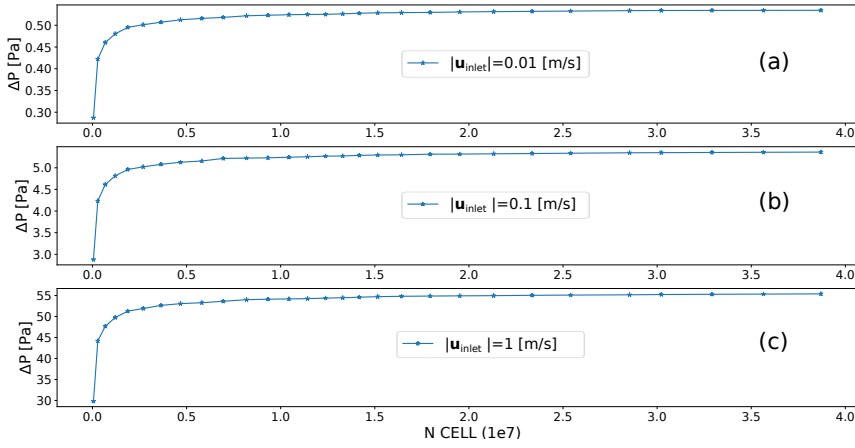
Fig. 11 Mesh convergence analysis of the digitalized Calcarb domain Fig. 9 characterized by three different inlet velocity values. The pressure difference between the inlet and the outlet is studied as the number of cells within the domain increases. Due to a different scaling in the pressure difference, cases a) and b) correspond to the creeping regime, whereas case c) to the inertial one.
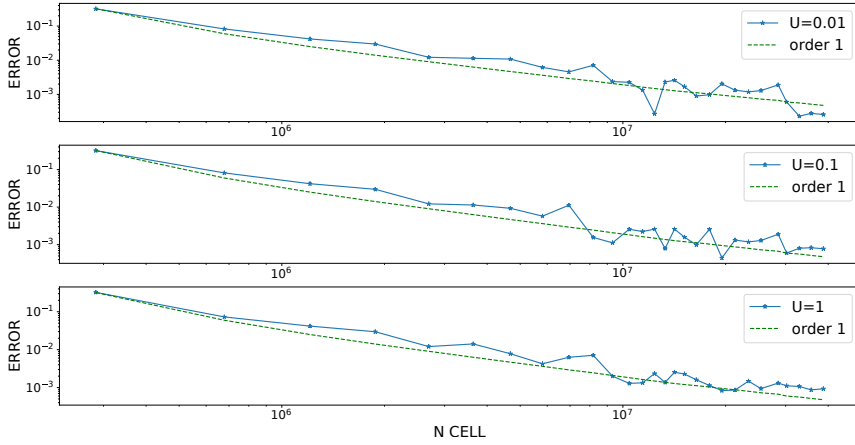
Fig. 12 Relative error convergence analysis of the digitalized Calcarb domain Fig. 9 characterized by three different inlet velocity values. Cases a) and b) correspond to the creeping regime, whereas case c) to the inertial one. Lines with first order slopes have been plotted to show the convergence order of the numerical method.

the pressure difference results are similar and just scaled between the two different velocities due to the linearity of the Stokes problem. However, as the velocity increases, case c), the appearance of inertial effect leads to different pressure difference relationships, thus scaling the value is no longer sufficient (see detailed investigation for numerous inlet velocities in the next section). Simulations a) and b) capture the creeping regime; simulations c) captures the inertial regime. The mesh convergence analysis is then performed for both
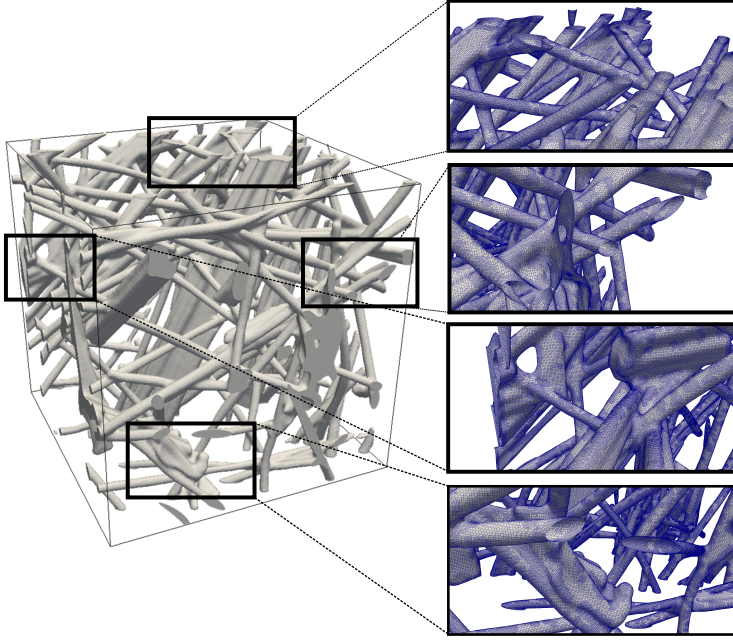
**Fig. 13** Some details of the meshed geometry. The final mesh accounts about 25 million cells.

regimes. Figure 12 shows the behaviour of the numerical error between two consecutive simulations

$$error = \frac{\Delta P_{n+1} - \Delta P_n}{\Delta P_{n+1}} \tag{11}$$

where the index $n + 1$ indicates the numerical simulation with more mesh refinement. In the figure the green lines have first order slopes. The numerical methods is then first order with respect to the discretization. The errors decay until they stabilize around 10^{-3} and 10^{-4} when the grid-size reaches the image resolution (2.6 μm). Based on this observation we have decided to select the 2 million cells-mesh to proceed with the computation of the permeability tensor. Some details of the meshed geometry are shown in Fig. 13

4.2 Permeability Tensor

The objectives of this section are two-fold: compute the permeability tensor of the Calcarb sample and investigate the validity of Darcy's law corresponding to the creeping regime at the pore-scale. The strategy has been applied for different values of the inlet velocity. A chosen from the analysis detailed in previous sections. The computed permeability components are presented in Fig. 14. It is possible to notice that when the inlet velocities are higher than
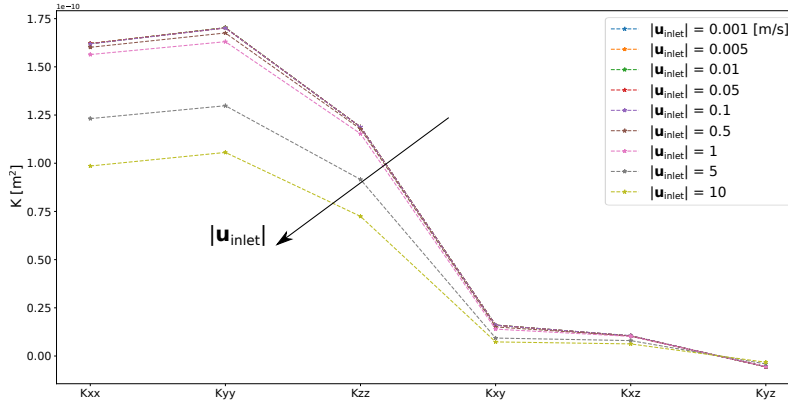
Fig. 14 Permeability components of the digitalized Calcarb domain by varying the inlet velocity.

$0.1\ m/s$, the components of the permeability start to decrease. This is due to the appearance of non-linearity effects. As said in Section 2.1, in order to take those effects into account at the macroscopic scale, the Forchheimer correction should be considered. However, for velocities lower than $0.1\ m/s$, the flow is in the creeping regime and the predicted tensor is constant and equal to

$$\underline{\underline{K}} = \begin{bmatrix} 1.56\ 10^{-10} & 1.39\ 10^{-11} & 1.02\ 10^{-11} \\ 1.39\ 10^{-11} & 1.63\ 10^{-10} & -5.4\ 10^{-12} \\ 1.02\ 10^{-11} & -5.4\ 10^{-12} & 1.15\ 10^{-10} \end{bmatrix}\ m^2 \tag{12}$$

where the average of the extra-diagonal terms $\left(\frac{K_{xy}+K_{yx}}{2},\ \frac{K_{xz}+K_{zx}}{2},\ \text{and}\ \frac{K_{zy}+K_{yz}}{2}\right)$ have been considered to force tensor symmetry. The obtained permeability tensor characterizes just the domain considered and not the whole material and this makes really difficult to check the results. However, this domain has already been studied by Borner et al, 2017 [13], by using a different approach[1] and by making several simplifications, reducing the tensor to just two scalars: in-plane and through-thickness components. In order to compare results of Eq. (12) a diagonalization procedure is required in order to write the tensor aligned to the principal axes of rotation

$$\underline{\underline{K}}_{dg} = \begin{bmatrix} 1.74\ 10^{-10} & 0 & 0 \\ 0 & 1.49\ 10^{-10} & 0 \\ 0 & 0 & 1.11\ 10^{-10} \end{bmatrix}\ m^2 \tag{13}$$

and results have a relative difference around 42% with respect to the prediction obtained by Borner et al, 2017 [13].

---

[1] The computation of the permeability is based on Monte Carlo simulations.

4.3 Characteristic Length of the Domain

As seen before, the relative importance between inertial and viscous forces within a fluid is characterized by the Reynolds number (Eq. (3)). Once defined, this parameter allows the determination of the flow regime hence which equations must be considered for its resolution. The problem is that a characteristic length ℓ needs to be defined and this choice is not trivial [69]. Both macroscopic and microscopic information can be considered for its determination and in this article we propose a new method based on the latter. This new technique is based on the vorticity vector, which is defined as

$$\boldsymbol{\omega} = \nabla \times \boldsymbol{u} \tag{14}$$

It describes the tendency of a flow to rotate. For an incompressible flow this field is governed by the following equation[2]

$$\frac{D\boldsymbol{\omega}}{Dt} = (\boldsymbol{\omega} \cdot \nabla)\boldsymbol{u} + \nu\nabla^2\boldsymbol{\omega} \tag{15}$$

Vorticity is therefore generated close to boundaries where velocity gradients contribute to the stretching/tilting term (the first source term at the second-hand side). Once generated, the vorticity diffuses into the entire domain due to the diffusion term. Due to the linear behaviour of the velocity, the vorticity increases proportional to the magnitude of the velocity in the creeping regime since the source term remains the same. However, as soon as the creeping regime falls, non-linearities in the velocity field change this simple trend. So, a simple way to check the validity of the creeping regime is to keep under observation the mean value of the vorticity over the whole domain. To investigate the loss of proportionality of the velocity (linear dependence on velocity) which exists in the creeping regime, it is possible to consider the dimensionless vorticity, defined as

$$\boldsymbol{\omega}^* = \boldsymbol{\omega}\frac{\ell}{U} \tag{16}$$

whose mean value remains constant in the creeping regime.
In order to illustrate this concept, let's apply it to the 1-sphere unit cell case showed in Fig. 3a with a high porosity value ($\epsilon = 0.875$) to simulate the case of flow around a sphere. This is a well-known case and according to a Reynolds number computed with respect to the diameter of the sphere, the limit for the creeping regime is usually set between 0.1 and 0.5 according to different authors [4,9,43]. As done in section 4.2 for the Calcarb geometry, let's first evaluate the permeability value of the high porosity 1-sphere porous medium for different Reynolds numbers. Then, based on those values, a limit for the creeping regime can be indirectly estimated by plotting the evolution of the estimated permeability or of the drag. A change in the slope indicates the appearance of inertial effect [4,9,43]. The limit can be inferred by directly

---

[2] The vorticity equation has been derived by taking the curl of the transient momentum equation.

Re	0.001	0.01	0.1	0.5	1	10	100
K^*	0.09911	0.09911	0.09912	0.09918	0.09939	0.11471	0.17641
ΔK^*	/	0.00 %	0.010 %	0.071 %	0.283 %	15.74 %	77.99 %
$|\boldsymbol{w}^*|$	3.985e+06	3.985e+06	3.985e+06	3.984e+06	3.982e+06	3.801e+06	3.2116e+06
$\Delta|\boldsymbol{w}^*|$	/	0.00 %	0.003 %	0.025 %	0.070 %	4.63 %	19.42 %

Table 4 Results for the high porosity 1-sphere porous medium case (Fig. 3a) with different Reynolds number in terms of permeability and mean vorticity over the domain. The Δ values refer to the quantity difference with respect to the lowest inlet Reynolds case.

Re_{avg}	0.01	0.05	0.1	0.5	1	5	10	50	100
ΔK^*	/	0.00	0.005 %	0.008 %	0.1 %	1.2 %	3.52 %	24.0 %	47.1 %
$\Delta|\boldsymbol{w}|^*$	/	0.00	0.005 %	0.009 %	0.11 %	0.65 %	0.97 %	3.93 %	7.51 %

Table 5 Permeability and mean vorticity variation for the Calcarb geometry as function of different inlet magnitude velocities. The Δ values refer to the quantity difference with respect to the lowest inlet Reynolds case.

evaluating for each simulation the mean vorticity value in the domain. This technique has the additional advantage of requiring fewer simulations. Results are shown in Table 4, where the diameter of the sphere has been considered as the characteristic length of the domain for the Reynolds numbers. As it is possible to see, both the permeability and vorticity start to change for $Re = 0.1$, but a significant variation can be really appreciated after $Re = 1$. So, depending on the precision desired, the creeping regime limit could be set at different Reynolds. One of the main advantages of this method is the fact that it is possible to identify in the domain the area where the vorticity presents its maximum values, that is, where non-linearity effects affect more the flow. In other words, it points to the area of the domain that is first subject to a transition to a different flow behaviour. This area could be considered as the physics-based characteristic length of the domain. In this case of the high porosity 1-sphere porous medium, the vorticity technique identifies the sphere area, leading to a characteristic length equal to the sphere diameter, as expected.

Let's now apply the same method to the Calcarb geometry. Results are shown in Table 5. The average pore-size length presented in Section 4, $\ell_{avg} = 135\ \mu m$, has been considered as the characteristic length for the computed Reynolds number denoted Re_{avg}. In the table Δ is taken as the difference of the quantity between a given simulation and the lowest Reynolds case. Based on the Δ values it is possible to set the limit for the creeping regime as Re_{avg} between 1 and 5, depending on the acceptable tolerance. As previously done, the vorticity can be now used to locate the portions of the domain where non-linearities effects are dominant. By progressively increasing the velocity in the domain it is possible to observe that the dimensionless vorticity field assumes its maximum values mainly inside a specific area in the domain[3]. This area is showed in Fig. 15 where on the right it is enlarged and the first obstacle found in the upwind direction is highlighted in red: a cluster of fibers with diameter

---

[3] For the moment the method is based on a qualitative analysis of the vorticity field. More analysis with different geometries should be performed to make the analysis more rigorous.
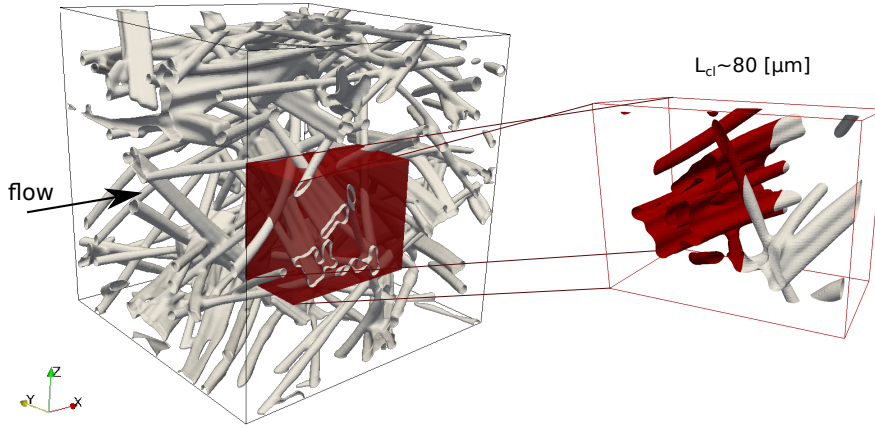
$L_{cl} \sim 80 \ [\mu m]$

flow

Fig. 15 Calcarb dataset characterized in this article, with a red box to highlight a small area that influences the behaviour of the flow inside the whole domain.

$\ell_{cl} \sim 80 \ \mu m$.

A verification on the vorticity analysis is given by a direct observation of the flow behaviour. By referring to the left of Fig. 15, let's assume a flow is coming along the x direction. About halfway through the domain, the flow faces the big cluster of fibers highlighted in red in Fig. 15. When velocities are small enough, the flow overtakes the cluster without any particular problem and therefore continues towards the outlet; with the increase of velocities, a part of the flow close to the right boundary ($Y = 0$) starts to move towards the center of the domain. This behaviour becomes more and more marked with increasing Reynolds as showed in Fig. 16; when $Re_{avg} \sim 10$, two counter-rotating vortices are formed in the area downstream of the cluster. So, the flow close to the right boundary, first overtakes the cluster, then feeds the vortices, and finally spreads towards the center of the domain; by further increasing Reynolds, the high-vorticity flow from the back of the cluster spreads the non-linearity effects all over the domain and this leads to the formation of different vortices. Therefore, the area downstream of the cluster is found to trigger the transition to inertial regime for the whole domain. This cluster of fibers is the same found through the vorticity field analysis, with a diameter of $\ell_{cl} \sim 80 \ \mu m$. By recalling the average pore-size length $\ell_{avg} = 135 \ \mu m$ presented in Section 4, it can be easily noticed that the red box is characterized by a cluster size that is nearly half of the pore domain average.

This analysis allows taking into account the real arrangement of the fibres inside the domain, however, it is limited to a specific case and with a different sample all the procedure should be repeated.

The Reynolds number can be defined by using ℓ_{cl} and thus the limits of the creeping regime [1,19] expressed as

$$Re_{cl} < 0.5 \longrightarrow creeping \ \ regime$$
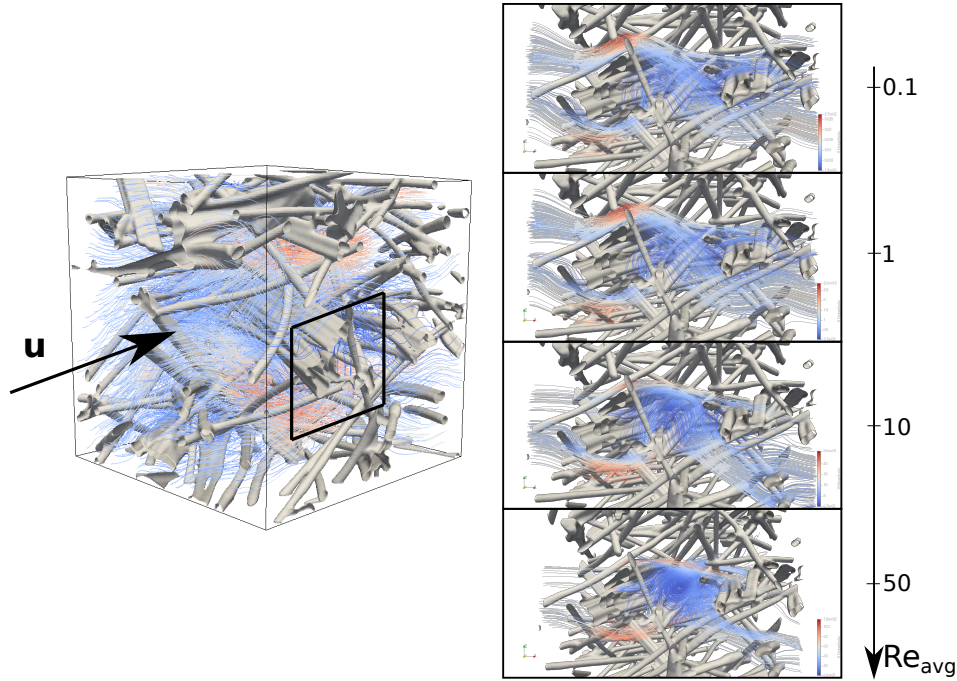
Fig. 16 Streamlines visualization in the domain and zoom on the characteristic area of the domain with flow behaviour at different Reynolds number. Streamlines are colored based on the velocity magnitude.

It should be remarked that this technique investigates the limit of the creeping regime, that is the weak inertial regime [1] where flows are no longer fully viscous but still steady. Thanks to it, we are able to provide a physical limit to the applicability of this study in the estimation of the permeability tensor. Future analysis and developing on this technique are however necessary.

5 Conclusions

In this work, a numerical strategy has been defined in order to characterize the dynamic interaction between a flow and a generic anistoropic non-periodic porous material. Specific attention was paid to the definition of the computational domain and the boundary conditions by defining different strategies and comparing their results on simple test cases. Both periodic and non-periodic geometries were considered in order to be as generic as possible. The selected strategy is based on the direct resolution of the Navier-Stokes equations under the assumption of creeping flow in order to estimate the physical quantities that appear in Darcy's law and leave the permeability tensor as the only unknown. In order to close the system and obtain all the components of the tensor three pore-scale numerical simulations need to be considered. Pore-scale

simulations in the real geometry bring numerous information such as pressure gradients and velocity fields. All this information has been used in this article to introduce a criterion for delimiting the creeping regime with the onset of the inertial regime. This criterion is based on the vorticity field and it has been verified and applied to the high porosity 1-sphere porous medium and to the Calcarb dataset. As showed in the results, the limit strongly depends on the error tolerance chosen to be acceptable. The analysis of vorticity was also adopted to define a physics-based characteristic length in the domain which has been used to define the Reynolds number and its value corresponding to the onset of the inertial regime. This criterion can be used to train deep learning techniques in the process of automatic identification of the physics-based characteristic length in a generic domain. The numerical framework that has been developed during this study is available in the Porous material Analysis Toolbox based on OpenFoam (PATO) released Open Source by NASA (www.pato.ac).

Conflict of interest

The authors declare that they have no conflict of interest.

6 Appendix A. Remarks on the Volume Averaging Method

This appendix has the only purpose to introduce the concepts of the volume averaging method used in this article. Further details can be found in the literature [67].

The volume averaging is a technique used to derive continuum-macroscopic equations for multiphase systems. In this way the complexity of a porous medium is replaced with an equivalent porous-continuum model in which each point is characterized by the properties of a representative elementary volume (REV) centered on it. Within this REV variables can be averaged. Two different definitions of averages have been adopted: the phase average which in this article has been used for the pressure term

$$P = \frac{1}{V_f} \int_{V_f} p \, dV \tag{17}$$

and the intrinsic average, used for the velocity field

$$\boldsymbol{U} = \frac{1}{V_{REV}} \int_{V_f} \boldsymbol{u} \, dV \tag{18}$$

Inside the REV each variable can be decomposed (Gray's decomposition [28]) as the summation of its average plus a deviation contribution. For the pressure field this decomposition is as follow

$$p = P + \tilde{p} \tag{19}$$

7 Appendix B. KclosureSolver

KclosureSolver is a solver implemented in PATO to solve the closure problem Eq. (20). By following the work of Anguy and Bernanrd, (1994) [6], transients terms have been added to the system to improve its stability. The desired solution is taken at the steady-state. An artificial compressibility, c, and an artificial viscosity coefficient, μ_{art}, are also introduced. The modified transient problem is as follows

$$\begin{cases} \dfrac{\partial \underline{\underline{d}}}{\partial t} + \nabla e - \nabla^2 (\mu_{art}\,\underline{d}) = \underline{I} & in \ \ V \\ \dfrac{\partial e}{\partial t} + c^2 \nabla \cdot \underline{d} = 0 & in \ \ V \\ BC1 : \underline{d} = 0 & at \ \ A_{fs} \\ BC2 : \underline{\underline{d}}(\boldsymbol{r} + l_i) = \underline{d}(\boldsymbol{r}), \ \ e(\boldsymbol{r} + \boldsymbol{l_i}) = e(\boldsymbol{r}) & i = 1, 2, 3 \end{cases} \tag{20}$$

The two equations are solved sequentially. Each equation can be iterated in a loop. The time integration is carried out through an implicit scheme.

8 Appendix C. Mesh Convergence Test Cases

In section 3, numerical simulations on six test cases are presented. The mesh refinement has been selected after a convergence analysis. By considering the 1-sphere unit cell with porosity $\epsilon = 0.55$, results of the convergence study with strategy A1 are presented in Table 6. The error% is evaluated taking into

N Cells	2414	11795	34099	74352	138911	233039	362489	533190
Error %	2.72	1.37	1.02	0.66	0.56	0.01	0.01	/
V_{ratio}	5.431 e-4	6.8 e-5	2.0 e-5	8.5e-6	4.3 e-6	2.5 e-6	1.6 e-6	1.1 e-6

Table 6 Mesh Convergence analysis with strategy A1 for the 1-sphere unit cell case defined in Section 3 with constant porosity $\epsilon = 0.55$. The error% is evaluated with respect to the result of the finer mesh. V_{ratio} is the ratio between the volume of the biggest finite-volume cell in the domain and the domain itself.

account the permeability estimation of two consecutive simulations as follows

$$error\% = 100\,\frac{|K_{Finer\_Mesh} - K_{Coarser\_Mesh}|}{K_{Finer\_Mesh}} \tag{21}$$

The quantity V_{ratio} is the ratio between the volume of the biggest cell in the domain and the domain itself. From the results in the table we can see that the convergence of the mesh is immediately achieved since the error is always decreasing by increasing the refinement. This trend, however, should stop when the tolerances of the simulation are reached. That is what happens in the table for the most refined meshes. The resolution of the mesh with 233039-cells can be then selected for the analysis in section 3.

References

1. Agnaou, M., Lasseux, D., Ahmadi, A.: Origin of the inertial deviation from darcy's law: An investigation from a microscopic flow analysis on two-dimensional model structures. Physical Review E **96**(4), 043105 (2017)
2. Ahrens, J., Geveci, B., Law, C.: Paraview: An end-user tool for large data visualization. The visualization handbook **717** (2005)
3. Ali, M., Umer, R., Khan, K., Cantwell, W.: Application of x-ray computed tomography for the virtual permeability prediction of fiber reinforcements for liquid composite molding processes: A review. Composites Science and Technology **184**, 107828 (2019)
4. Almedeij, J.: Drag coefficient of flow around a sphere: Matching asymptotically the wide trend. Powder Technology **186**(3), 218–223 (2008)
5. Andrä, H., Combaret, N., Dvorkin, J., Glatt, E., Han, J., Kabel, M., Keehm, Y., Krzikalla, F., Lee, M., Madonna, C., et al.: Digital rock physics benchmarks—part i: Imaging and segmentation. Computers & Geosciences **50**, 25–32 (2013)
6. Anguy, Y., Bernard, D., Ehrlich, R.: The local change of scale method for modelling flow in natural porous media (i): Numerical tools. Advances in water resources **17**(6), 337–351 (1994)
7. Antohe, B., Lage, J., Price, D., Weber, R.: Experimental determination of permeability and inertia coefficients of mechanically compressed aluminum porous matrices (1997)
8. Ashari, A., Bucher, T., Tafreshi, H.V.: A semi-analytical model for simulating fluid transport in multi-layered fibrous sheets made up of solid and porous fibers. Computational materials science **50**(2), 378–390 (2010)
9. Bagheri, G., Bonadonna, C.: On the drag of freely falling non-spherical particles. Powder Technology **301**, 526–544 (2016)
10. Barrere, J., Gipouloux, O., Whitaker, S.: On the closure problem for darcy's law. Transport in Porous Media **7**(3), 209–222 (1992)
11. Bernard, D., Nielsen, Ø., Salvo, L., Cloetens, P.: Permeability assessment by 3d interdendritic flow simulations on microtomography mappings of al–cu alloys. Materials Science and Engineering: A **392**(1-2), 112–120 (2005)
12. Bodla, K., Murthy, J., Garimella, S.: Microtomography-based simulation of transport through open-cell metal foams. Numerical Heat Transfer, Part A: Applications **58**(7), 527–544 (2010)
13. Borner, A., Panerai, F., Mansour, N.: High temperature permeability of fibrous materials using direct simulation monte carlo. International Journal of Heat and Mass Transfer **106**, 1318–1326 (2017)
14. (Brochure), M.: Calcarb rigid carbon thermal insulation (2017). Https://www.mersen.com/sites/default/files/publications-media/3-gs-calcarb-grade-cbcf-18-2000-mersen.pdf
15. Chamsri, K., Bennethum, L.: Permeability of fluid flow through a periodic array of cylinders. Applied Mathematical Modelling **39**(1), 244–254 (2015)
16. Cushman, J., Bennethum, L., Hu, B.: A primer on upscaling tools for porous media. Advances in Water Resources **25**(8-12), 1043–1067 (2002)
17. Davy, C., Adler, P.: Three-scale analysis of the permeability of a natural shale. Physical Review E **96**(6), 063116 (2017)
18. Derossi, A., Gerke, K., Karsanina, M., Nicolai, B., Verboven, P., Severini, C.: Mimicking 3d food microstructure using limited statistical information from 2d cross-sectional image. Journal of food engineering **241**, 116–126 (2019)

19. Dybbs, A., Edwards, R.: A new look at porous media fluid mechanics—darcy to turbulent. In: Fundamentals of transport phenomena in porous media, pp. 199–256. Springer (1984)
20. Dyck, N., Straatman, A.: A new approach to digital generation of spherical void phase porous media microstructures. International Journal of Heat and Mass Transfer **81**, 470–477 (2015)
21. Forchheimer, P.: Wasserbewegung durch boden. Z. Ver. Deutsch, Ing. **45**, 1782–1788 (1901)
22. Gerke, H.: Preferential flow descriptions for structured soils. Journal of Plant Nutrition and Soil Science **169**(3), 382–400 (2006)
23. Gerke, K., Karsanina, M., Katsman, R.: Calculation of tensorial flow properties on pore level: Exploring the influence of boundary conditions on the permeability of three-dimensional stochastic reconstructions. Physical Review E **100**(5), 053312 (2019)
24. Gerke, K., Karsanina, M., Skvortsova, E.: Description and reconstruction of the soil pore space using correlation functions. Eurasian soil science **45**(9), 861–872 (2012)
25. Gerke, K., Korost, D., Vasilyev, R., Karsanina, M., Tarasovskii, V.: Studying structure and determining permeability of materials based on x-ray microtomography data (using porous ceramics as an example). Inorganic Materials **51**(9), 951–957 (2015)
26. Gerke, K.M., Sizonenko, T.O., Karsanina, M.V., Lavrukhin, E.V., Abashkin, V.V., Korost, D.V.: Improving watershed-based pore-network extraction method using maximum inscribed ball pore-body positioning. Advances in Water Resources **140**, 103576 (2020)
27. Gerke, K.M., Vasilyev, R.V., Khirevich, S., Collins, D., Karsanina, M.V., Sizonenko, T.O., Korost, D.V., Lamontagne, S., Mallants, D.: Finite-difference method stokes solver (fdmss) for 3d pore geometries: Software development, validation and case studies. Computers & geosciences **114**, 41–58 (2018)
28. Gray, W.: A derivation of the equations for multi-phase transport. Chemical Engineering Science **30**(2), 229–233 (1975)
29. Guibert, R., Horgue, P., Debenest, G., Quintard, M.: A comparison of various methods for the numerical evaluation of porous media permeability tensors from pore-scale geometry. Mathematical Geosciences **48**(3), 329–347 (2016)
30. Haussener, S., Coray, P., LipiĹ, W., Wyss, P., Steinfeld, A., et al.: Tomography-based heat and mass transfer characterization of reticulate porous ceramics for high-temperature processing. Journal of Heat Transfer **132**(2), 023305 (2010)
31. Issa, R.: Solution of the implicitly discretised fluid flow equations by operator-splitting. Journal of computational physics **62**(1), 40–65 (1986)
32. Jaganathan, S., Tafreshi, H.V., Pourdeyhimi, B.: Two-scale modeling approach to predict permeability of fibrous media. Journal of Engineered Fibers and Fabrics **3**(2), 155892500800300208 (2008)
33. Jobic, Y., Kumar, P., Topin, F., Occelli, R.: Determining permeability tensors of porous media: A novel 'vector kinetic'numerical approach. International Journal of Multiphase Flow **110**, 198–217 (2019)
34. Khan, Z.A., Elkamel, A., Gostick, J.T.: Efficient extraction of pore networks from massive tomograms via geometric domain decomposition. Advances in Water Resources **145**, 103734 (2020)
35. Kumar, P., Topin, F.: Investigation of fluid flow properties in open cell foams: Darcy and weak inertia regimes. Chemical Engineering Science **116**, 793–805 (2014)
36. Lachaud, J., Mansour, N.: Porous-material analysis toolbox based on openfoam and applications. Journal of Thermophysics and Heat Transfer **28**(2), 191–202 (2014)
37. Lachaud, J., Meurisse, J.: Http://pato.ac/
38. Lachaud, J., Scoggins, J., Magin, T., Meyer, M., Mansour, N.: A generic local thermal equilibrium model for porous reactive materials submitted to high temperatures. International Journal of Heat and Mass Transfer **108**, 1406–1417 (2017)
39. Landis, E., Keane, D.: X-ray microtomography. Materials characterization **61**(12), 1305–1316 (2010)
40. Liakopoulos, A.: Darcy's coefficient of permeability as symmetric tensor of second rank. Hydrological Sciences Journal **10**(3), 41–48 (1965)
41. Manwart, C., Aaltosalmi, U., Koponen, A., Hilfer, R., Timonen, J.: Lattice-boltzmann and finite-difference simulations for the permeability for three-dimensional porous media. Physical Review E **66**(1), 016702 (2002)

42. Masad, E., Al Omari, A., Chen, H.C.: Computations of permeability tensor coefficients and anisotropy of asphalt concrete based on microstructure simulation of fluid flow. Computational Materials Science **40**(4), 449–459 (2007)
43. Mikhailov, M., Freire, A.: The drag coefficient of a sphere: An approximation using shanks transform. Powder technology **237**, 432–435 (2013)
44. Moreira, E., Innocentini, M., Coury, J.: Permeability of ceramic foams to compressible and incompressible flow. Journal of the European Ceramic Society **24**(10-11), 3209–3218 (2004)
45. Mustard, J., Adler, M., Allwood, A., Bass, D., Beaty, D., Bell, J., Brinckerhoff, W., Carr, M., Des Marais, D., Brake, B., et al.: Report of the mars 2020 science definition team. Mars Explor. Progr. Anal. Gr **150**, 155–205 (2013)
46. Panerai, F., Ferguson, J., Lachaud, J., Martin, A., Gasch, M., Mansour, N.: Micro-tomography based analysis of thermal conductivity, diffusivity and oxidation behavior of rigid and flexible fibrous insulators. International Journal of Heat and Mass Transfer **108**, 801–811 (2017)
47. Panerai, F., White, J., Cochell, T., Schroeder, O., Mansour, N., Wright, M., Martin, A.: Experimental measurements of the permeability of fibrous carbon at high-temperature. International Journal of Heat and Mass Transfer **101**, 267–273 (2016)
48. Patankar, S., Spalding, D.: A calculation procedure for heat, mass and momentum transfer in three-dimensional parabolic flows. In: Numerical prediction of flow, heat transfer, turbulence and combustion, pp. 54–73. Elsevier (1983)
49. Petrasch, J., Meier, F., Friess, H., Steinfeld, A.: Tomography based determination of permeability, dupuit–forchheimer coefficient, and interfacial heat transfer coefficient in reticulate porous ceramics. International Journal of Heat and Fluid Flow **29**(1), 315–326 (2008)
50. Pickup, G., Ringrose, P., Jensen, J., Sorbie, K.: Permeability tensors for sedimentary structures. Mathematical Geology **26**(2), 227–250 (1994)
51. Piller, M., Schena, G., Nolich, M., Favretto, S., Radaelli, F., Rossi, E.: Analysis of hydraulic permeability in porous media: from high resolution x-ray tomography to direct numerical simulation. Transport in porous media **80**(1), 57 (2009)
52. Quintard, M.: Introduction to heat and mass transport in porous media. Porous media interaction with high temperature and high speed ows, STO-AVT-261. VKI p. 33 (2015)
53. Ranut, P., Nobile, E., Mancini, L.: High resolution microtomography-based cfd simulation of flow and heat transfer in aluminum metal foams. Applied thermal engineering **69**(1-2), 230–240 (2014)
54. Renard, P., Genty, A., Stauffer, F.: Laboratory determination of the full permeability tensor. Journal of Geophysical Research: Solid Earth **106**(B11), 26443–26452 (2001)
55. Rocha, R., Cruz, M.: Calculation of the permeability and apparent permeability of three-dimensional porous media. Transport in porous media **83**(2), 349–373 (2010)
56. Sahimi, M.: Flow and transport in porous media and fractured rock: from classical methods to modern approaches. John Wiley & Sons (2011)
57. module by Simpleware, F.: Http://www.simpleware.com/
58. Soulaine, C., Gjetvaj, F., Garing, C., Roman, S., Russian, A., Gouze, P., Tchelepi, H.: The impact of sub-resolution porosity of x-ray microtomography images on the permeability. Transport in porous media **113**(1), 227–243 (2016)
59. Stackpoole, M., Sepka, S., Cozmuta, I., Kontinos, D.: Post-flight evaluation of stardust sample return capsule forebody heatshield material. In: 46th AIAA Aerospace Sciences Meeting and Exhibit, p. 1202 (2008)
60. Straatman, A., Gallego, N., Yu, Q., Betchen, L., Thompson, B.: Forced convection heat transfer and hydraulic losses in graphitic foam. Journal of heat transfer **129**(9), 1237–1245 (2007)
61. Tranter, T., Gostick, J., Burns, A., Gale, W.: Capillary hysteresis in neutrally wettable fibrous media: a pore network study of a fuel cell electrode. Transport in porous media **121**(3), 597–620 (2018)
62. Valvatne, P.H., Blunt, M.J.: Predictive pore-scale modeling of two-phase flow in mixed wet media. Water resources research **40**(7) (2004)
63. Van Doormaal, M., Pharoah, J.: Determination of permeability in fibrous porous media using the lattice boltzmann method with application to pem fuel cells. International journal for numerical methods in fluids **59**(1), 75–89 (2009)

64. Vu, J., Straatman, A.: Comparison of pore-level and volume-averaged computations in highly conductive spherical-void-phase porous materials. Transport in Porous Media **124**(2), 509–531 (2018)
65. Whitaker, S.: Flow in porous media i: A theoretical derivation of darcy's law. Transport in porous media **1**(1), 3–25 (1986)
66. Whitaker, S.: The forchheimer equation: a theoretical development. Transport in Porous media **25**(1), 27–61 (1996)
67. Whitaker, S.: The method of volume averaging, vol. 13. Springer Science & Business Media (2013)
68. Wiegmann, A.: Computation of the permeability of porous materials from their microstructure by fff-stokes. Bericht des Fraunhofer ITWM **129** (2007)
69. Wood, B., He, X., Apte, S.: Modeling turbulent flows in porous media. Annual Review of Fluid Mechanics **52**, 171–203 (2020)
70. Wright, M., Beck, R., Edquist, K., Driver, D., Sepka, S., Slimko, E., Willcockson, W.: Sizing and margins assessment of mars science laboratory aeroshell thermal protection system. Journal of Spacecraft and Rockets **51**(4), 1125–1138 (2014)
71. Xiong, Q., Joseph, C., Schmeide, K., Jivkov, A.: Measurement and modelling of reactive transport in geological barriers for nuclear waste containment. Physical Chemistry Chemical Physics **17**(45), 30577–30589 (2015)